

## Multi-Aspect Solutions for Moving Vehicle Testing

Dr. S. Fonov\*, Dr. J. Crafton, Dr. L. Goss, Dr. G. Jones, Dr. V. Fonov

ISSI  
Dayton, OH 45440  
USA

\* [sfonov@innssi.com](mailto:sfonov@innssi.com)

Dr. C. Tyler

WPAFRL VA, Dayton, OH

[Charles.Tyler@wpafb.af.mil](mailto:Charles.Tyler@wpafb.af.mil)

### ABSTRACT

*This paper reviews an integrated testing approach for investigating the effects of fluid dynamic phenomena on the performance of moving vehicles and their models. This approach is based upon the combination of advanced optical diagnostic techniques with computational fluid dynamic models to provide a comprehensive understanding of a vehicle's aerodynamic and hydrodynamic performance. Advanced optical diagnostic techniques that will be discussed include: pressure sensitive paint (PSP - surface flow visualization, aerodynamic loads), temperature sensitive paint (TSP - temperature map and heat transfer), surface stress sensitive films ( $S^3F$  - pressure and shear force maps), and stereovideogrammetry (model movement under loading). The current "state of the art" of these techniques allows to develop integrated systems approach for aerodynamic testing which includes: hardware, acquisition-analysis software, and a comprehensive comparison with CFD predictions.*

### 1.0 INTRODUCTION

Traditional techniques for acquiring measurements of surface temperature and pressure on wind tunnel models have utilized embedded arrays of thermocouples and pressure taps. This approach requires significant model construction and setup time while producing data with limited spatial resolution. Furthermore, physical constraints such as mechanical movement or section thickness can preclude the use of thermocouples and pressure taps in certain regions of a model. An alternative approach that has received considerable attention over the past 15 years is the use of luminescent probes that are sensitive to temperature and pressure. These techniques, known as Temperature and Pressure-Sensitive Paint, have resulted in high spatial resolution measurements of temperature and pressure on surfaces that have proven in the past to be inaccessible<sup>1</sup>.

While Pressure-Sensitive Paints (PSP) have demonstrated significant potential in high-speed wind tunnels, several issues that limit the accuracy of the technique have been identified [1,2,3]. Among these issues are errors due to model displacement and deformation, instability of the illumination source, photo-degradation and sedimentation of the painted surface, and non-uniform temperatures on the model surface. Errors in PSP measurements have prevented wide deployment of PSP systems for numerous industrial applications. An approach that eliminates the errors in PSP measurements would provide a significant benefit for research and result in wider acceptance of the PSP technique.

Fonov, S.; Crafton, J.; Goss, L.; Jones, G.; Fonov, V.; Tyler, C. (2005) Multi-Aspect Solutions for Moving Vehicle Testing. In *Recent Developments in Non-Intrusive Measurement Technology for Military Application on Model- and Full-Scale Vehicles* (pp. 5-1 – 5-32). Meeting Proceedings RTO-MP-AVT-124, Paper 5. Neuilly-sur-Seine, France: RTO. Available from: <http://www.rto.nato.int/abstracts.asp>.

# Report Documentation Page

Form Approved  
OMB No. 0704-0188

Public reporting burden for the collection of information is estimated to average 1 hour per response, including the time for reviewing instructions, searching existing data sources, gathering and maintaining the data needed, and completing and reviewing the collection of information. Send comments regarding this burden estimate or any other aspect of this collection of information, including suggestions for reducing this burden, to Washington Headquarters Services, Directorate for Information Operations and Reports, 1215 Jefferson Davis Highway, Suite 1204, Arlington VA 22202-4302. Respondents should be aware that notwithstanding any other provision of law, no person shall be subject to a penalty for failing to comply with a collection of information if it does not display a currently valid OMB control number.

1. REPORT DATE <b>01 APR 2005</b>		2. REPORT TYPE <b>N/A</b>		3. DATES COVERED <b>-</b>	
4. TITLE AND SUBTITLE <b>Multi-Aspect Solutions for Moving Vehicle Testing</b>				5a. CONTRACT NUMBER	
				5b. GRANT NUMBER	
				5c. PROGRAM ELEMENT NUMBER	
6. AUTHOR(S)				5d. PROJECT NUMBER	
				5e. TASK NUMBER	
				5f. WORK UNIT NUMBER	
7. PERFORMING ORGANIZATION NAME(S) AND ADDRESS(ES) <b>Dayton, OH 45440 USA</b>				8. PERFORMING ORGANIZATION REPORT NUMBER	
9. SPONSORING/MONITORING AGENCY NAME(S) AND ADDRESS(ES)				10. SPONSOR/MONITOR'S ACRONYM(S)	
				11. SPONSOR/MONITOR'S REPORT NUMBER(S)	
12. DISTRIBUTION/AVAILABILITY STATEMENT <b>Approved for public release, distribution unlimited</b>					
13. SUPPLEMENTARY NOTES <b>See also ADM202216., The original document contains color images.</b>					
14. ABSTRACT					
15. SUBJECT TERMS					
16. SECURITY CLASSIFICATION OF:			17. LIMITATION OF ABSTRACT	18. NUMBER OF PAGES	19a. NAME OF RESPONSIBLE PERSON
a. REPORT <b>unclassified</b>	b. ABSTRACT <b>unclassified</b>	c. THIS PAGE <b>unclassified</b>			

## Multi-Aspect Solutions for Moving Vehicle Testing

---

The concept of image based measurements model displacement and deformation is not unique [4]. In fact, measurements of pressure using PSP and deformation have been successfully demonstrated [5]. The direct measurement of model geometry has several benefits. Utilization of image based measurements of temperature or pressure requires that the two-dimensional image be mapped onto the three-dimensional geometry for comparison to computational models. Furthermore, the direct measurement of the experimental geometry is of significant value when comparing theoretical or computational results to actual experimental measurements. A system capable of performing simultaneous measurements of pressure and model geometry would be of significant value.

The hardware platform for each of these techniques includes a surface or volume distributed transducer, a specialized light source, an image acquisition system and dedicated acquisition and analysis software. Data processing algorithms includes many identical steps like image alignment using cross-correlation techniques, image resection, and image filtering - restoration steps.

## 2.0 EXPERIMENTAL FACILITIES

The UCAV experiments were performed in the SARL wind tunnel at Wright-Patterson Air Force Base, a schematic of the SARL wind tunnel is given in Figure 1. The SARL is an open-circuit, low-speed wind tunnel with a 3.05 meter by 2.13 meter test section and a maximum Mach number of 0.5. The tunnel provides excellent optical access with Pyrex windows on both the top and each side of the test section.

The Boeing UCAV model, shown in Figure 2, is a hybrid design built by John Hopkins University Applied Physics Laboratory. The model is composed of an internal metal structure to withstand the aerodynamic loading and an external geometry constructed using a rapid-prototype stereo-lithography polymer. The model has a lambda wing with a span of approximately 4 feet and length of 3 feet. Control surfaces on the trailing edge were adjusted to  $-20$ ,  $0$ , and  $+20$  degrees for the current tests. The angle of attack was varied from  $0$  to  $20$  degrees and measurements were conducted at Mach numbers of  $0.2$  and  $0.4$ .

The UCAV model was provided by Dr. Charles Tyler who conducted both computational (second order three-dimensional Euler simulation) and traditional experimental studies (i.e. aerodynamic force and moments, pressure taps) of the flow field associated with this model. Results from the PSP and SVMD experiments are to be compared to these experimental and computational results. Again, the goal of this program is to develop new experimental tools for rapid evaluation of aerodynamic designs and validation of CFD predictions.

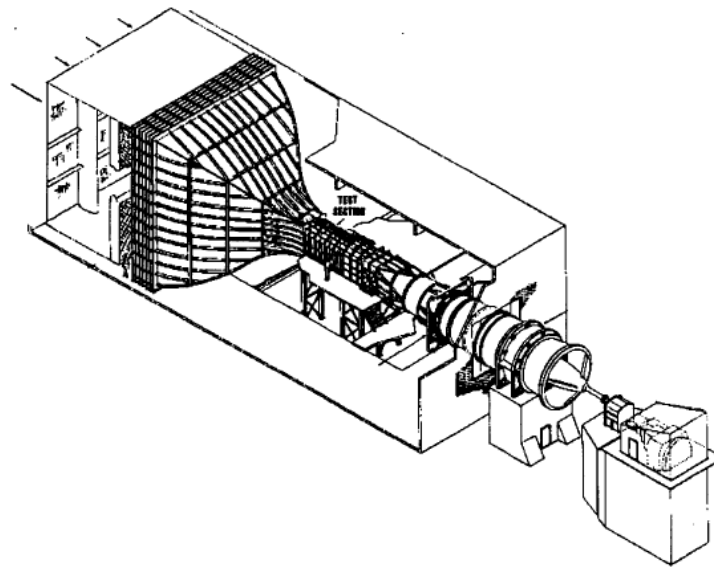


Figure 1: SARL wind tunnel.

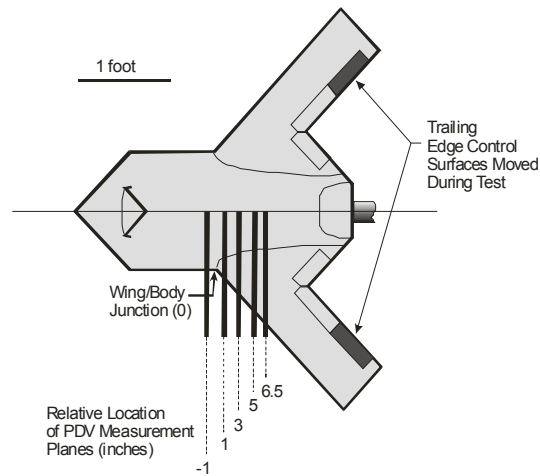


Figure 2: Boeing UCAV Model.

Low speed PSP and S3F measurements were conducted at ISSI low speed wind tunnel. Wind tunnel has test section with dimensions 10” by 4” and provides flow with velocity 0 - 20m/s and 38 - 45m/s.

### 3.0 PRESSURE-SENSITIVE PAINT

A typical pressure sensitive paint is composed of two main parts, an oxygen-sensitive fluorescent molecule, and an oxygen permeable binder. The pressure sensitive paint method is based on the sensitivity of certain luminescent molecules to the presence of oxygen. When a luminescent molecule absorbs a photon, it transitions to an excited singlet energy state. The molecule then typically recovers to the ground state by the

## Multi-Aspect Solutions for Moving Vehicle Testing

emission of a photon of a longer wavelength. In some materials oxygen can interact with the molecule such that the transition to the ground state is non-radiative, this process is known as oxygen quenching. The rate at which these two processes compete is dependent on the partial concentration of oxygen present, with a higher oxygen concentration quenching the molecule more, thus giving off a lower intensity of light. Based on Henry's law, an increase in air pressure on the PSP surface gives a proportional increase in the oxygen concentration that provides possibility for surface pressure measurement.

Image based pressure measurements using PSP are accomplished by coating the model surface with the paint and illuminating the surface with light of the appropriate wavelength to excite the luminescent molecule. The surface is imaged through a long-pass filter to separate the luminescent signal from the excitation light and the luminescent signal distribution is recorded. A schematic of the system is shown in Figure 3. Unfortunately, the luminescent signal from the paint is not only a function of pressure. The luminescence varies with illumination intensity, probe concentration, paint layer thickness, and detector sensitivity. These spatial variations result in a non-uniform luminescent signal from the painted surface. The spatial variations are eliminated by taking the ratio of the luminescent intensity of the paint at an unknown test condition,  $I$ , with the luminescent intensity of the paint at a known reference condition,  $I_0$ . Using this *wind-on wind-off* ratio, the response of the system can be modeled using a modification of the Stern-Volmer equation.

$$P/P_0 \cong 1 + A(T) * (I_0 / I) + B(T) * (I_0 / I)^2 \quad (1)$$

where the subscript "o" refers to a reference "wind-off condition". The functions A and B are properties of a particular paint system and local paint temperature.

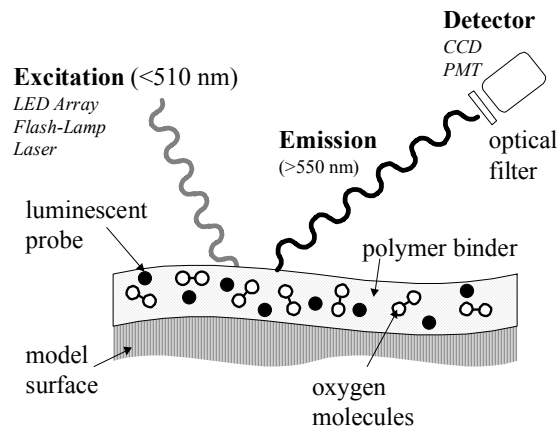


Figure 3: Basic PSP system.

## 4.0 ERRORS IN PSP MEASUREMENTS

Detailed analysis of sources of uncertainty for PSP measurements can be found in Liu paper [2]. These error sources include temperature, illumination, model displacement/deformation, sedimentation, photo-degradation, and camera shot noise. Liu concluded that the major sources of error were temperature and illumination. These two sources of error will be discussed and the minimization of these errors through the use of binary PSP will be discussed. Errors due to temperature will be considered first.

Note in equation 1 that the Stern-Volmer coefficients,  $A(T)$  and  $B(T)$  are functions of temperature. The Stern-Volmer coefficients are temperature dependent because temperature affects both non-radiative deactivation and oxygen diffusion in a polymer. In fact, the temperature dependence of  $A(T)$  is due to thermal quenching while the temperature dependence of  $B(T)$  is related to the diffusivity of oxygen in a polymer binder. The temperature sensitivity of the Stern-Volmer coefficients are modeled following Liu as:

$$\begin{aligned}
 A(T) &= A(T_o) \left[ 1 + \frac{E_{nr}}{R T_o} \left( \frac{T - T_o}{T_o} \right) \right] \\
 B(T) &= B(T_o) \left[ 1 + \frac{E_p}{R T_o} \left( \frac{T - T_o}{T_o} \right) \right]
 \end{aligned}
 \tag{2}$$

Temperature sensitivity can lead to errors in converting the intensity distributions to pressure. This is demonstrated by considering a calibration of a PSP composed of Platinum tetra(pentafluorophenyl)porphine (PtTFPP) in Fluoro/Isopropyl/Butyl (FIB), shown in Figure 4. The quantity  $I_o/I$  is a monotonic function of pressure along each isotherm. The *wind-on* and *wind-off* images however, must be acquired at the same temperature if the conversion to pressure is to be free from temperature errors. A second temperature related issue is the slope of the curve along each isotherm. For most PSP's, the slope of the sensitivity curve is a function of temperature. An accurate measurement of the absolute temperature is necessary to correctly convert the intensity ratio to pressure. An important property of the PtTFPP/FIB paint is the property of ideality<sup>6</sup>. For an ideal paint, the slope of the sensitivity curve is independent of temperature. This property is of significant value for minimizing temperature errors in PSP measurements. It is also a significant advantage in the production of a temperature compensating Binary PSP.

For radiometric PSP, errors in pressure measurements due to temperature are largely the result of changes in the temperature of the model surface between the acquisition of the *wind-off* and *wind-on* image. However, any temperature gradient on the model surface will still result in a temperature-induced error in the pressure measurements. These temperature gradients can be the result of model construction, tunnel operation, or fluid dynamics. The UCAV model is constructed using an internal metal structure and a polymer resin. The thermal signature of the internal structure is apparent when the surface of the model is subjected to a heat flux. The model is commonly exposed to a heat flux due to changes in tunnel Mach number. This condition is most apparent during tunnel startup. While the model will eventually reach equilibrium with the tunnel, productivity requires that data acquisition continue and elimination of temperature errors will provide a significant increase in data accuracy under these conditions. Even after the model has reached thermal equilibrium the temperature distribution on the model is not necessarily uniform. One example of a temperature gradient generated by the external flow is boundary layer transition. In this case, one must consider the recovery temperature defined as:

$$T_r = T + \frac{V^2}{2 C_p} r
 \tag{3}$$

In this equation,  $T_r$  is the recovery temperature,  $T$  is the static temperature,  $V$  is the fluid velocity,  $C_p$  is the specific heat of the fluid, and  $r$  is the recovery factor. The recovery factor for a boundary layer with no pressure gradient is a function of Prandtl number and the state of the boundary layer. According to White<sup>7</sup>, this relationship is:

$$\begin{aligned}
 r &= \sqrt{\text{Pr}} = 0.841 \Rightarrow \textit{lam.} \\
 r &= \sqrt[3]{\text{Pr}} = 0.891 \Rightarrow \textit{turb.}
 \end{aligned}
 \tag{4}$$

Using equation 3 and equation 4 and assuming a Mach number of 0.4, boundary layer transition should result in a temperature gradient of about 0.5 degrees Kelvin. The UCAV model is constructed from a low thermal conductivity material therefore the boundary condition is close to adiabatic. The temperature gradient will be close to the 0.5 Kelvin but the model surface will reach a steady state temperature quickly. Assuming the temperature sensitivity of PtTFPP/FIB, this temperature gradient will produce an error in pressure of 0.1 psi.

The relationship between surface illumination and paint luminescence is linear; therefore, any change in surface illumination will result in an equal change in paint luminescence. Errors in pressure measurements

Multi-Aspect Solutions for Moving Vehicle Testing

caused by variations in surface illumination can stem from several sources. Consider utilizing a point source for the illumination of a surface as shown in Figure 5. The relationship between illumination intensity at a point on the surface and the distance between the source and the point of interest are an inverse function of the distance squared. Any movement of the painted surface or illumination source will result in a change in the distance between these two points, and thus a change in the illumination intensity at the surface. This movement can result from deformation of the model surface, or physical displacement of the model or illumination source. Another source of illumination errors is the temporal stability of the illumination source. Any variation of the intensity of the illumination source between the *wind-off* and *wind-on* images will register as an error in illumination.

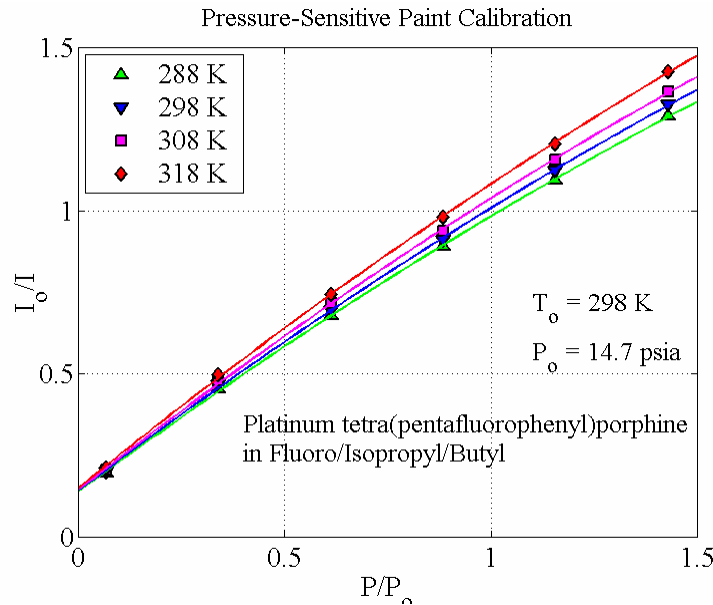


Figure 4: Calibration of PtTFPP/FIB.

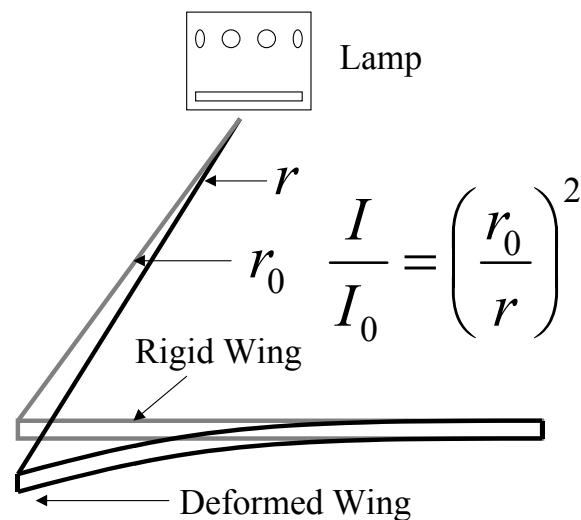


Figure 5: Error due to illumination.

## 5.0 BINARY PRESSURE-SENSITIVE PAINT

One means of dealing with the issue of illumination errors is to employ a reference probe, in fact, several groups have successfully demonstrated this approach [8,9]. The goal is to use the luminescence of the reference probe to correct for variations in the luminescence of the signal probe (the pressure sensor) that is due to variations in illumination. This is accomplished by taking a ratio of the luminescence of the signal probe to the luminescence of the reference probe. Assuming that both the signal and probes response is linearly proportional to the local illumination and probe number density the resulting function is:

$$R(P, T, n_s, n_r) = \frac{F_s(P, T) n_s I}{F_r(P, T) n_r I} \quad (5)$$

The dependence of R on illumination has been removed, however R is still a function of temperature, pressure, and the concentration of each probe. If the distributions of the signal and reference probes are identical, the dependence on probe concentration is removed. This condition however, is difficult to achieve. To eliminate the effects of probe concentration, the standard *wind on* and *wind off* ratio (a ratio of ratios) is applied.

$$S(P, T) = \frac{R_0(P_0, T_0) \frac{n_s}{n_r}}{R(P, T) \frac{n_s}{n_r}} = \frac{R_0(P_0, T_0)}{R(P, T)} \quad (6)$$

The system response S is now a function of pressure and temperature only. At first glance, this ratio of ratios procedure may not seem to be an improvement over the standard radiometric approach. However, the relative concentration of each probe is static therefore only a single *wind-off* is needed. This is a significant improvement in tunnel productivity as it reduces the number of test conditions by a factor of two.

Selection of the reference probe is by no means trivial. The reference probe must be excited by the same illumination source that is used to excite the signal probe and the luminescence of the reference probe must be spectrally separated from the luminescence of the signal probe. The reference probe must be compatible with the solvents and binders that are used for the signal probe. Finally to maximize the pressure sensitivity of the system, the reference probe should exhibit as little sensitivity to pressure as possible. A paint that meets these criteria is known as a Self-Referencing Paint.

With illumination removed from equation 6 the goal becomes minimizing the sensitivity of the system to temperature. The approach utilized involves allowing the reference probe, which is eliminating sensitivity to illumination, to compensate for the temperature sensitivity as well. This is accomplished by adding two constraints to the selection criteria already outlined for a self-referencing paint:

- 1) The combination of the signal probe and paint binder must form an ideal paint and
- 2) The temperature sensitivity of the reference probe must match the temperature sensitivity of the ideal paint.

A PSP composed of PtTFPP/FIB is a good candidate for a binary paint. PtTFPP/FIB is an ideal paint with low temperature sensitivity. A binary PSP composed of PtTFPP/FIB and a selected reference probe has been used to produce a PSP with low temperature sensitivity. The calibration of this paint is shown in Figure 7. The temperature sensitivity of ISSI Binary FIB is less than 0.05% per degree K over a range of temperatures from 5°C to 45°C and pressures from 1 to 20 psia.

The effectiveness of the binary PSP system for elimination of errors caused by temperature and illumination is demonstrated by two experimental measurements. Using the ISSI Binary FIB [9] Bell performed pressure measurements on an airfoil at low speed. Using only the pressure channel of the binary paint, Bell noted that the pressure distribution was compromised. However, reprocessing the data using the reference channel corrected the data and provided pressure measurements that agreed with the in-situ taps to better than five thousands of a psi. This data is shown in Figure 8. A second demonstration of the ISSI binary PSP involved the measurements of pressure on a UCAV in the SARL at WPAFB shown in Figure 9. Again,

Multi-Aspect Solutions for Moving Vehicle Testing

errors caused by model movement and temperature are minimized and effective measurements of pressure using PSP technology are demonstrated.

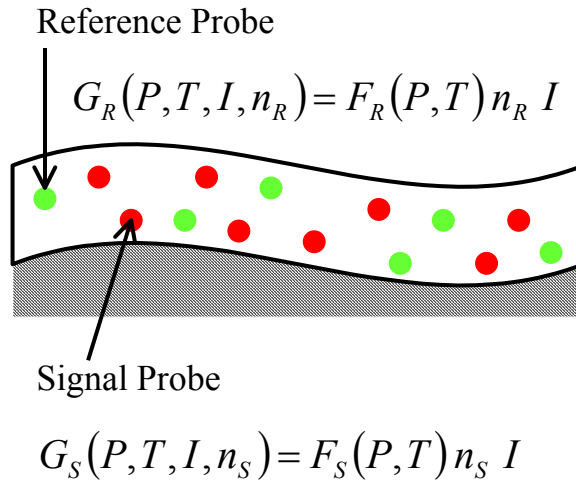


Figure 6: Binary Pressure-Sensitive Paint.

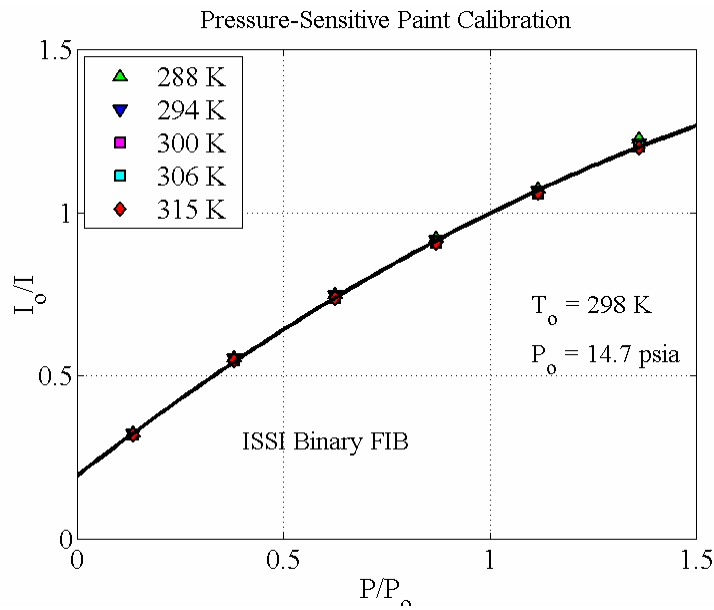


Figure 7: Calibration of ISSI Binary FIB.

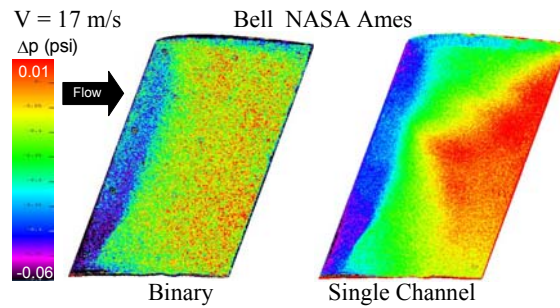


Figure 8: Comparison of Single and Binary Paint pressure distributions at low speed.

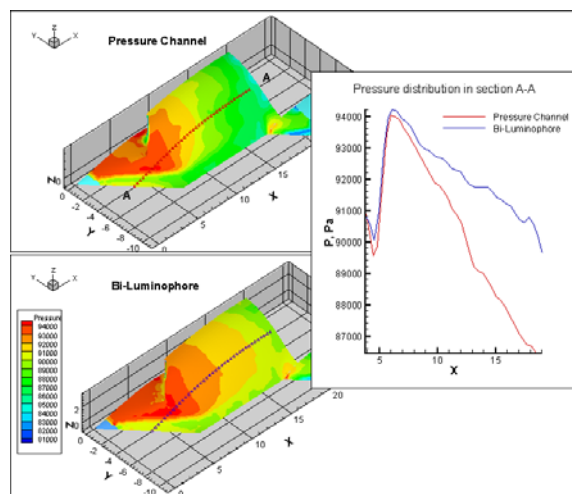


Figure 9: Comparison of Single and Binary Paint pressure distributions.

## 6.0 S<sup>3</sup>F MEASUREMENT TECHNIQUE

It is necessary to emphasize that PSP's based on the oxygen quenching are essentially absolute pressure gage. PSP sensitivity  $dI/I/dP$  is a function of the pressure level and dramatically decreasing as  $1/P^2$  that implies additional problems.

Sensitivity  $d(I_0/I)/dP$  for most currently available PSP formulation varies in the range (50% -100%)/Bar and can not be increased significantly due to physical and photochemical properties of available formulations what creates problems for PSP applications where pressure variations are small [11,12]. Typical example is pressure field measurements at low subsonic velocities – Mach number below 0.05. Pressure variation on the model is proportional to squared Mach number. It means that pressure variation range  $\delta P$  for  $Ma=0.05$  ( $V=35$ mile/h) is about 100Pa that is hundred time less then at  $M=0.5$  ( $V=350$ mile/h and  $\delta P=10^4$ Pa) but PSP sensitivity can't be modified in the such scale and only one possibility to get reliable result is increasing of the signal to noise ratio in the acquired information (usually images) and compensating all disturbing factors like illumination non-stability, model displacement and deformation, temperature effects. PSP temperature sensitivity varies between  $100Pa/^\circ C$  to  $1000Pa/^\circ C$  that is comparable with total pressure variation range for  $Ma=0.05$ . Finally PSP measurements at flow velocities below  $Ma=0.05$  are semi-quantitative up to now and require significant efforts.

Multi-Aspect Solutions for Moving Vehicle Testing

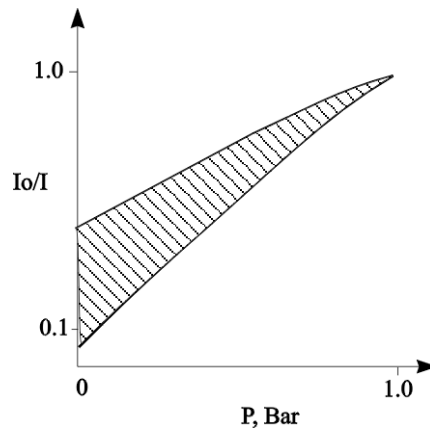


Figure 10: Stern-Vormer approximation of PSP signal.

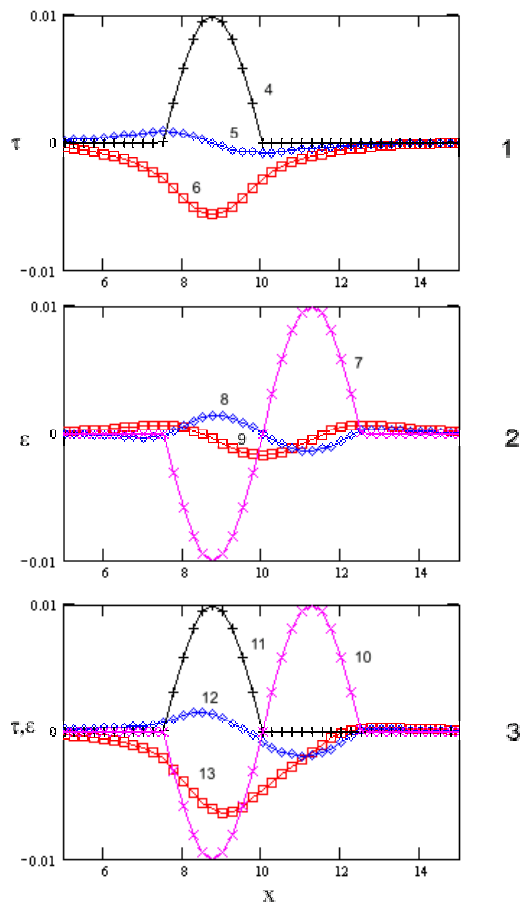


Figure 11: FEA of action of shear force (Plot 1), normal force (Plot 2) and their combination (Plot 3).

Mapping of the shear stresses is accomplished using liquid crystals or different approaches with oil film measurements [10, 13, 14]. At the beginning of nineties method for direct measurements of surface shear force was offered [15, 16]. Method includes mount on the model surface of sensing element in the form of film made of flexible material-polymer gel of desired thickness with known shear modulus; markers are applied to film and model surfaces, and shear deformation of film caused by flow is measured by interference method; shearing stress is determined using Hooke's law for shear strain. Markers may be made in the form of reflection grating placed on model surface (under film) and transmitting grating on film surface enabling use of moiré phenomenon for recording shear strain. Method provides improved accuracy and informative capacity due to determining local values of shearing stress. The main drawback of this method is connected with the fact that gradients of the normal pressure creates shear displacement of polymer gel as well and method will work well only in the absence of normal pressure gradients [19]. This is demonstrated by results of Finite Elements Analysis presented in Figure 11, cases 1, 2 and 3.

Case 1. Shear force 4 with amplitude 100Pa which is applied at the surface of polymer gel having thickness 1mm, shear module  $\mu=600\text{Pa}$  and Poisson ratio  $\nu=0.496$ , creates shear deformation 6 accompanied by normal deformation 5 (referred to gel thickness 1mm).

Case 2. The same layer under action of the normal pressure distribution 7 having amplitude 100Pa. Shear and normal deformations are presented as distributions 9 and 8.

Case 3. Combination of loads from cases 1 and 2. Shear deformation 13 is determined by joint action of normal and shear forces and calculation of the shear force distribution will require information about normal force as well. It is worth mentioned that normal deformations are less sensitive to the shear force action. Practically interesting cases in flow investigations are characterized by regions with large pressure pikes and pressure gradients but usually shear forces and shear force gradients are 10...100 smaller that creates more difficult problem for recognition of input in shear deformation from normal and shear surface load components.

Standard approach to reach high measurement accuracy is increasing of the gage sensitivity with measuring only increments relative some etalon value located in measurement range – using for example differential pressure gage instead of absolute pressure gage. This is idea of differential pressure measurement is cornerstone of this method. Polymer behaves like non-compressible fluid but contrary standard fluid tries to recover original shape after removal of deformation force.

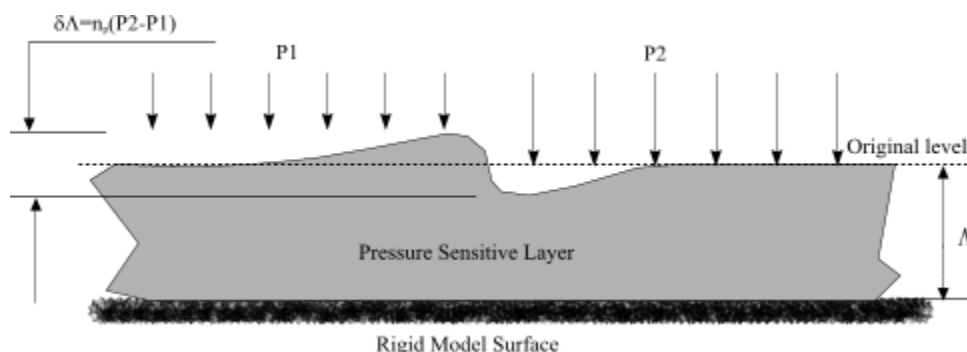


Figure 12: Realization of the Differential Principle.

Pressure loads P1 and P2 applied at adjacent surfaces will displace polymer material that resulted in change of the local layer thickness at value  $\delta\Lambda \sim n_p(P2-P1)$ . This is only crude scheme; in general deformations of the polymeric layer are governed by pressure gradients and shear force as well.

Range of linear frequency response of S3F is limited by natural frequency of shear oscillation and can be estimated as

## Multi-Aspect Solutions for Moving Vehicle Testing

$$f_0 = \frac{1}{2\pi} \sqrt{\frac{\mu}{\rho\Lambda^2}}$$

Changing  $\mu \in (100 \dots 1000) \text{Pa}$ , and  $\Lambda \in (0.1 \dots 1) \text{mm}$  it is possible to adjust frequency response in the range 0.3..10KHz that is approximately 100 times better than standard PSP based on oxygen quenching.

In order for a pressure sensitive film to produce desired results it must be applied on the surface under study. There are several ways for film applications like airbrush spraying and “shrink-fit method”. The last provides films with controlled thickness and useful for evaluation phase. Source components are poured into flat cavity having smoothed or even polished bottom. After polymerization the film is peeled of and placed on an airfoil. Film thickness can be estimated by direct measurements using for example optical absorption or capacitor type thickness gage. The next step is the film calibration. This procedure includes application of specified load on the film surface and measurements corresponding normal and tangential deformation distribution – evaluation of the film response functions. The smaller load application area the more film response function will corresponds to impulse function.

Consider for simplicity a 1D load application. In this case deformations can be treated in 2D space. Plate has a cavity with a rectangular cross-section  $[0,20] \times [0,1]$  The cavity is filled with S3F and the characteristic length ( $d=1 \text{ mm}$ ) is the thickness of the S3F. Concentrated constant loads (normal or tangential) are applied on the interval  $\{9.9, 10.1\}$ . Zero deformations on the cavity walls determine boundary conditions for this problem.

The S3F is an elastic solid and is deformed under the applied forces. A point in the solid, originally at  $(x,y)$  goes to  $(X,Y)$  upon application of the load. If the displacement vector  $\vec{r} = (r_1, r_2) = (X - x, Y - y)$  is small, Hooke’s law relates the stress tensor  $\sigma$  inside the solids to the deformation tensor  $\varepsilon$  [17]:

$$\sigma_{ij} = \lambda \delta_{ij} \nabla \cdot \vec{r} + \mu \varepsilon_{ij}, \quad \varepsilon_{ij} = \frac{1}{2} \left( \frac{\partial r_i}{\partial x_j} + \frac{\partial r_j}{\partial x_i} \right) \quad (7)$$

where  $\delta_{ij}$  is the Kronecker symbol ( $\delta_{ij} = 1$ , if  $i=j$ ,  $\delta_{ij} = 0$ , if  $i \neq j$ ), and  $\lambda, \mu$  are two Lamé constants describing the material mechanical properties in terms of the modulus of elasticity  $E$ , and Poisson ratio  $\nu$  as:

$$\lambda = \frac{E\nu}{(1+\nu)(1-2\nu)}, \quad \mu = \frac{E}{(1+2\nu)}.$$

The equation of elasticity are written in variation form for the displacement vector  $\vec{r}(x) \in \Omega$  as

$$\int_{\Omega} \left[ \mu \varepsilon_{ij}(\vec{r}) \varepsilon_{ij}(\vec{w}) + \lambda \varepsilon_{ii}(\vec{r}) \varepsilon_{ii}(\vec{w}) \right] = \int_{\Gamma} \vec{r} \cdot \vec{w}, \quad \forall \vec{w} \in \Omega \quad (8)$$

and the integrals are in volume  $\Omega$  or on volume boundary  $\Gamma$  [18].

Solution results are presented at Figure 13. Zoomed view of the deformed grid shows that deformations concentrated mainly in region with diameter about 2..3 thickness of the elastic layer.

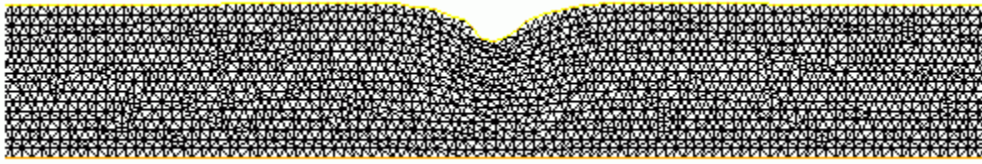


Figure 13: Solution of the problem (Zoomed view of the deformed FE grid).

Plots on Figure 14 present normal (blue line) and tangential (red line) displacements as result of action of the rectangular pulse load (pink line) on the layer surface. Magnitude of tangential displacement approximately two times more than magnitude of normal displacement on the region outside of applied load. So, information about tangential displacement can be used for normal force visualization as well. Of course normal displacements below load application region are significantly larger. This function of normal displacement distribution  $g(x)$  can be treated as reaction on the pulse load  $\delta(x)$ . Next assumption will be that elastic reaction  $\mathbf{R}(x) \equiv (R_x, R_y)$  on the arbitrary surface load  $\mathbf{L}(x) = (L_x, L_y)$  can be treated as a linear system<sup>17, 18</sup>:

$$\mathbf{R}(x) = \int \mathbf{G}(x - x') \mathbf{L}(x') dx' \quad (9)$$

Normal displacement reaction on action of the normal “pulse” force (Fig. 14) can be approximated by function:

$\tilde{n}_n(x) = \frac{1}{\mu} (a_0 + a_1 \exp(-|x|/k_1) + a_2 \exp(-|x|/k_2))$ , where parameters  $(k_1, k_2$  and  $a_i$  are obtained to minimize approximation error. Shear displacement reaction on action of normal “pulse” force is approximated by function  $\tilde{n}_s(x) = \frac{1}{\mu} (a_3 + a_4 \exp(-|x|/k_3))$

Similarly for case of shear “pulse” load, approximations for normal  $\tilde{s}_n$  and shear  $\tilde{s}_s$  reaction can be presented as:

$$\tilde{s}_n(x) = \frac{1}{\mu} (a_5 + a_6 \exp(-|x|/k_4)),$$

$$\tilde{s}_s(x) = \frac{1}{\mu} (a_7 + a_8 \exp(-|x|/k_5) + a_9 \exp(-|x|/k_6))$$

## Multi-Aspect Solutions for Moving Vehicle Testing

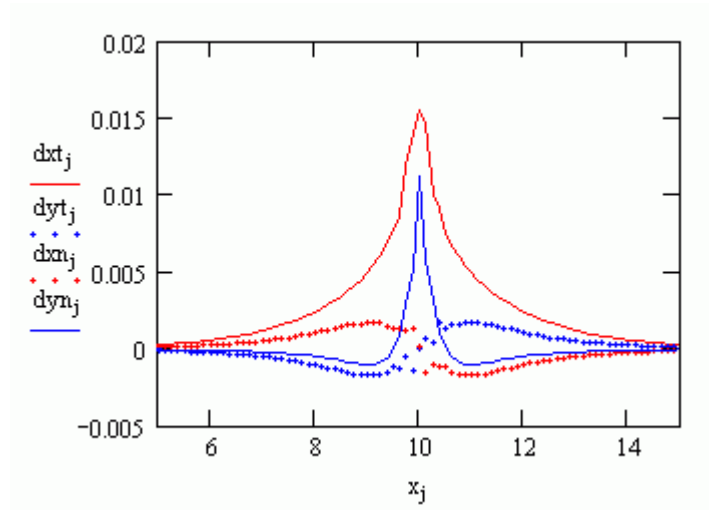


Figure 14: Displacements on the upper boundary, normal and shear loads 10 Pa, layer thickness  $h=1\text{mm}$ ,  $E=60.0$ ,  $\nu=0.498$ . Tangential displacement due to tangential load – red line, normal displacement due to normal load – blue line, red dotted line corresponds to normal displacement due to shear load and blue dotted line – shear displacement due to normal load.

Reaction on the arbitrary load  $L_j = (L_{nj}, L_{sj})$  applied at the interval  $[x_0, x_N]$  can be presented as:

$$R_{nj} = \Delta x \sum_{k=0}^N L_{nk} \tilde{n}_n(x_j - x_k) + L_{gk} \tilde{s}_n(x_j - x_k) \quad (10)$$

$$R_{sj} = \Delta x \sum_{k=0}^N L_{nk} \tilde{n}_s(x_j - x_k) + L_{gk} \tilde{s}_s(x_j - x_k)$$

This system of linear equations (10) relative unknown  $L_k$  has diagonally dominant matrix (Figure 15)

$\mathbf{G}_{jk} = \begin{pmatrix} \tilde{n}_{nj} & \tilde{s}_{nj} \\ \tilde{n}_{sj} & \tilde{s}_{sj} \end{pmatrix}$ , which can be inverted and solution of linear equations can be written as:

$$\mathbf{L} = \mathbf{G}^{-1} \cdot \mathbf{R} \quad (11)$$

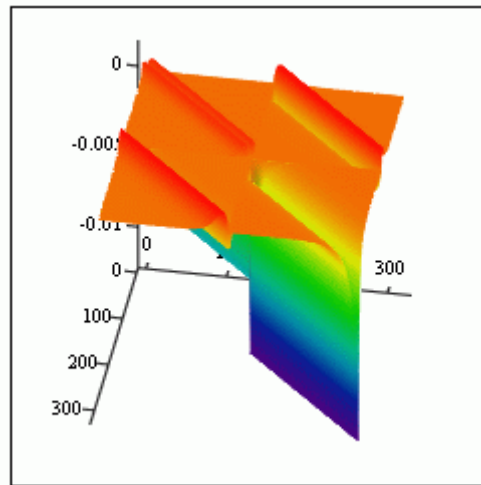


Figure 15: 3D presentation of G matrix.

Response functions depend on film thickness. Plots on Figure 16 present results of FEA modeling of response on harmonic normal and tangential loads applied on interval  $d$  on S3F with thickness  $d_1$ . Maximum deformations as function of  $d_1/d$  can be treated as measure of spatial Amplitude-Frequency Characteristics of S3F. AFC for normal load (red line) and tangential load are quite different especially at low  $d_1/d$  – low spatial frequency that provide possibility to adjust sensitivity for pressure and shear force measurements.

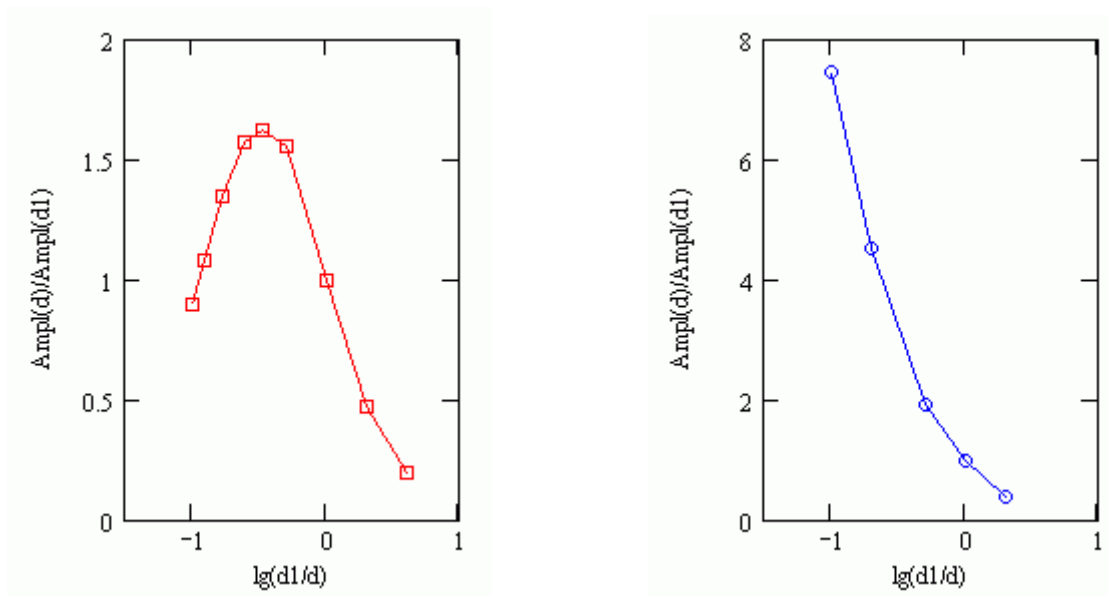


Figure 16: Estimation of AFC for normal (left) and tangential (right) loads.

## Multi-Aspect Solutions for Moving Vehicle Testing

General layout of image acquisition system for S3F measurements is presented in Figure 17. All three deformation components can be extracted from set of wind-off, wind-on images taken by one hi-resolution CCD camera. Normal component in this configuration is measured using luminescence signal from S3F. It requires stable light source and at least 12-bit amplitude resolution CCD camera. Dynamic measurements usually require pulsed light sources and reference channel to compensate exposure non stability and model displacements. Good approach in this case is using color CCD camera like Hamamatsu C7780 having 3 CCD chips for R, G and B channels. Reference signal in green region is created by luminescence from S3F substrate, information about normal deformation is acquired in red region and information about shear deformations is taken from blue region. Static measurements were conducted using QIMAGING RETIGA EX monochrome CCD camera having 1280 by 1024 pixel spatial resolution and 12-bit amplitude resolution or PCO camera having 1600 by 1200 pixel spatial and 14 bit amplitude in combination with ISSI LED lamps (output in 406nm or 460nm).

OMS 3.1 software package was used for image processing which include alignment of wind off and wind on images, normalizing, and calculation of the shear displacement fields. Software provides model displacement compensation as a rigid body using additional information from markers located on S3F substrate.

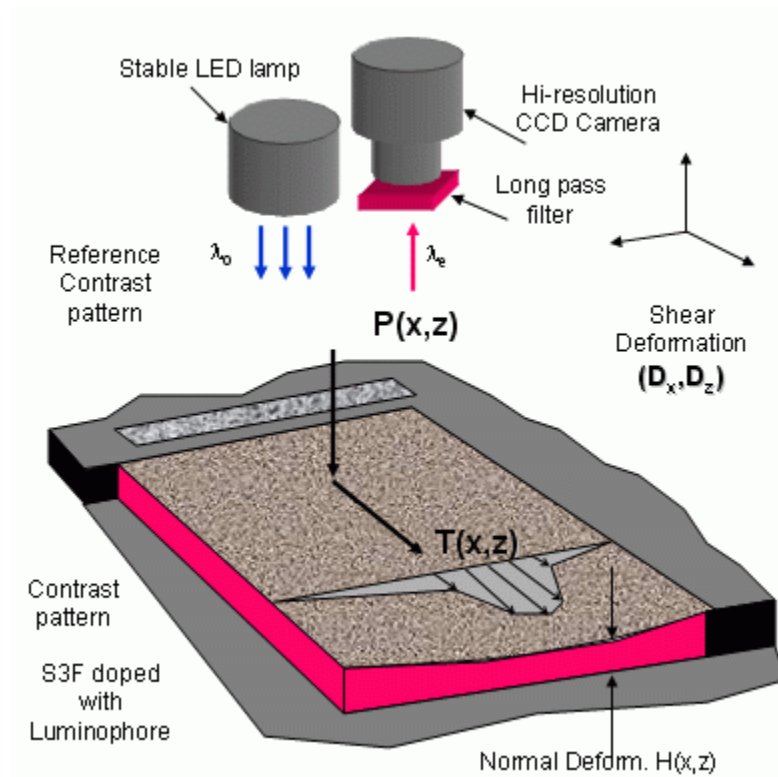


Figure 17: General Layout of S3F image acquisition system.

S3F sensitivity should be adjusted in accordance with dynamic range of surface forces taking into account limitation on maximum acceptable deformation of the surface under study due to possible influence on the flow itself. Usually relative normal deformations are below 1-2% (referred to the film thickness), film thickness is less than 1-10% of characteristic thickness of the model.

## 7.0 S<sup>3</sup>F EVALUATION TESTS

Shear Stress Module and film thickness are the main parameters determining sensitivity and spatial resolution of the S<sup>3</sup>F. Shear module  $\mu$  can be measured directly by applying shear force to the film with known thickness and measuring corresponding displacement. Response functions can be estimated using FEA model described before but some efforts were applied to verify FEA model itself. Practically it is possible to create stable PSF having shear stress module in the range  $\mu= 30 - 3000\text{Pa}$  and more. Plot on Fig.18 demonstrate calibration curve for practical S3F composition. Composition have good linearity and small hysteresis, which is in the range of tangential displacement measurement accuracy  $\sigma=0.1\text{-}0.3\mu\text{m}$ . Total linear dynamic range of the displacement is about  $1000\mu\text{m}$  that is large enough compared with S3F layer thickness  $1730\mu\text{m}$  for this case.

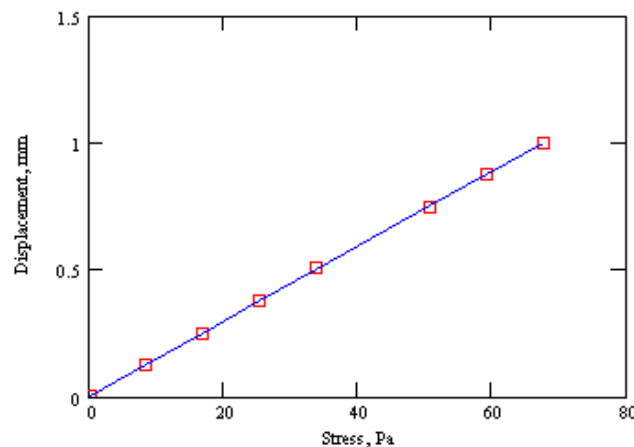


Figure 18: Calibration curve for S3F composition with shear stress module  $\mu=117\text{Pa}$ .

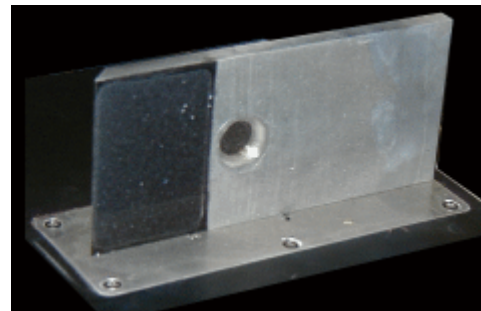
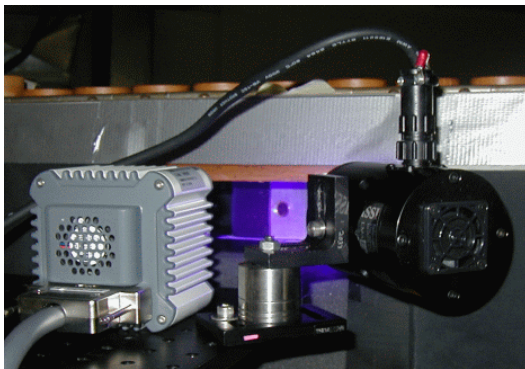


Figure 19: Typical experimental setup (Left). Tested model (Right)  
Cavity having depth 1mm (front black part) is filled with S3F.

The first try to use S3F for pressure field visualization demonstrated very promising results. Successful visualizations were conducted for flow velocity from parts of m/s to 1m/s (in water), and from 10m/s to 45m/s in airflow.

## Multi-Aspect Solutions for Moving Vehicle Testing

Simple models with known pressure and friction force distributions were used for the feasibility tests. One of such models is presented at Figure 19. This is plate having wedged leading edge installed vertically at test section floor at zero side angle. Plate has cavity near by leading edge filled with S3F. Flow velocity varied from 10 to 20m/s. Normal and shear deformation fields obtained at 20m/s are presented at Figures 20 and 21. Deformation field in the center line section can be considered as two dimensional and data recovery scheme described above can be used for this case. Plots (Figure 22) show comparison of measured pressure and friction force coefficients with CFD estimations.

Delta wing model (Figure 23) was tested at flow velocity range 5- 40m/s, angle of attack  $10^{\circ}$ - $15^{\circ}$ . Upper surface has cavity filled with S3F with the thickness 1mm. Fine  $TiO_2$  powder was applied on the upper surface of PSF to create pattern for shear deformation measurements. Similar model with PSP was tested to compare S3F-PSP data (Figure 24).

Field of the relative thickness distribution is presented at Figure 25. Vortex above wing surface creates narrow decompression region with pressure gradient oriented mainly across the ambient flow direction, so for each cross section elastic deformation problem can be treated as plane. Plot in Figure 26 is comparison of PSP and S3F data taken in approximately identical flow conditions. PSF sensitivity is about 25 times more and comparable SNR on the resulting image can be obtained by acquisition only 3 images instead of about 180 images for PSP.

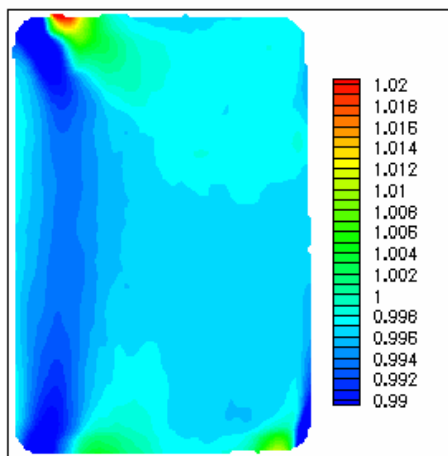


Figure 20: Normal deformation field.

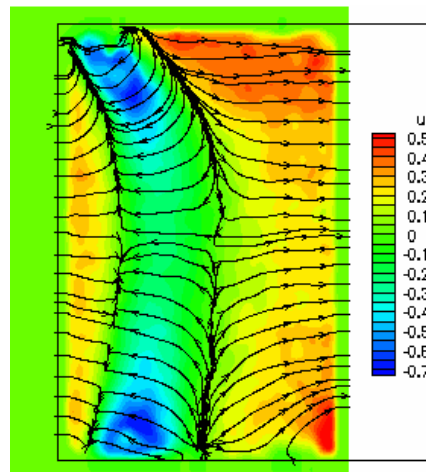


Figure 21: Shear deformation field.

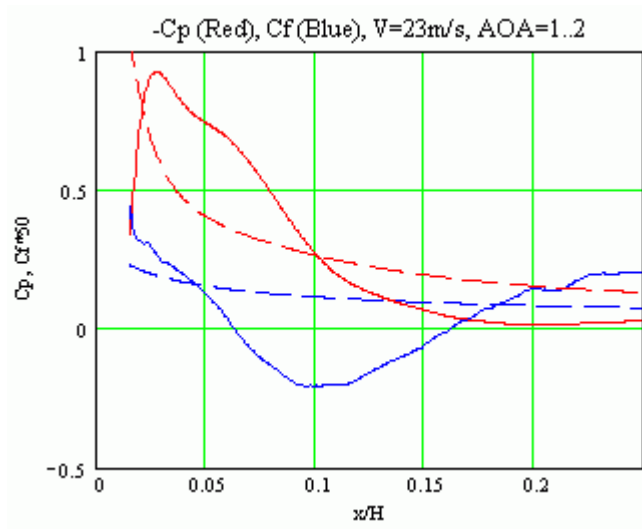


Figure 22: Reconstructed  $-C_p$  (red) and  $C_f \cdot 50$  (blue) distributions compared with CFD (2D potential flow) and Blasius estimations (dashed lines),  $V=23\text{m/s}$ , angle of attack  $\alpha \approx 1^\circ$ .

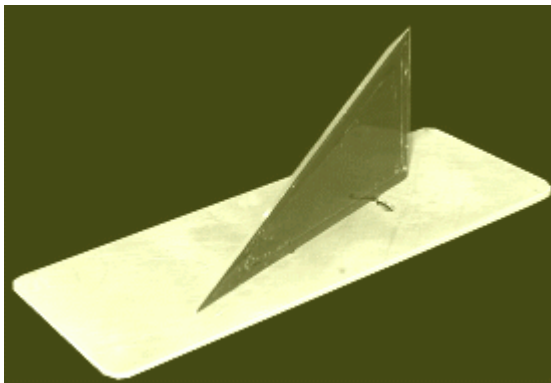


Figure 23: Delta wing model.

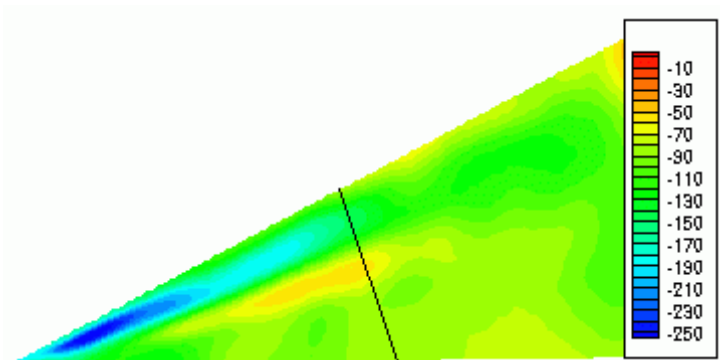


Figure 24: PSP results,  $V=15\text{m/s}$ ,  $\alpha=12^\circ$ .

## Multi-Aspect Solutions for Moving Vehicle Testing

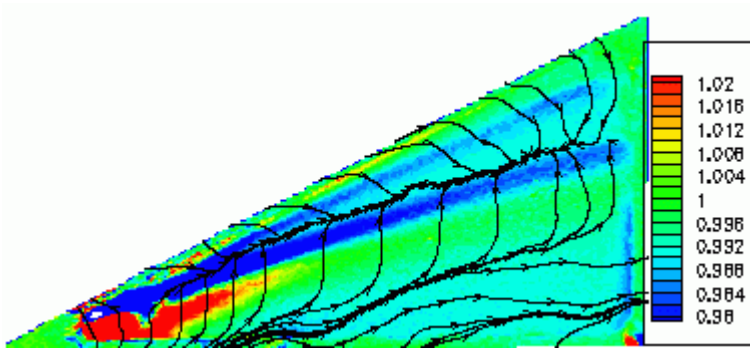


Figure 25: S3F results. Shear Displacement Vector Field and normal component of deformation field (false color presentation). Flow velocity 16m/s, angle of attack  $\alpha=10^\circ$ .

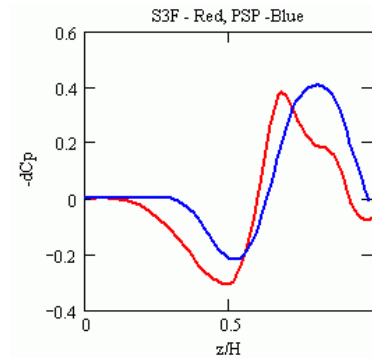


Figure 26: Comparison S3F ( $V=16\text{m/s}$ ,  $\alpha=10^\circ$ ) data with PSP ( $V=15\text{m/s}$ ,  $\alpha=12^\circ$ ) data.

## 8.0 STEREO PHOTOGRAMMETRY

Image based measurements in wind tunnels have been used to determine quantities such as model deformations and angle of attack [4,5]. It is desirable to combine measurements of pressure using PSP with model geometry to facilitate comparison of experimental and computational results. PSP may be implemented as an imaged-based technique. Obtaining three-dimensional information from plane images is accomplished using the principals of photogrammetry. It is noted that measurements of pressure using PSP and model geometry using Photogrammetry have been demonstrated. These measurements however, were accomplished using independent systems. In general, the information necessary for determining model geometry is contained within the PSP images. By applying photogrammetry principals to PSP images, a system has been developed for acquiring pressure and model geometry using the same images.

In general, 3D model geometry may be determined using at least two images taken with some angular and space parallax. Binary PSP requires two images of the model, a signal and reference image. While it is common to acquire these images using a single camera and a filter switch, two independent views of the model are also acceptable especially for short duration or transient processes. The latter approach is used in developing the combined Binary PSP Stereo Photogrammetry system.

General photogrammetry often requires a complex calibration process. A point at real world location  $(X_w, Y_w, Z_w)$  is projected onto the image plane of the camera at  $(X, Y)$ . If the exact position, orientation and objective lens distortion of each camera is known, the real world position of the point can be determined from projection relationships. However, precisely measuring the orientation and location of the cameras can be difficult. The method of photogrammetry instead uses a generalized matrix model to form a map from the camera image planes back to the real world coordinate system.

Calibration points are used to provide known locations in real space that correspond to certain known locations in the camera image planes. The cameras must all contain the calibration points within their field of view. For each calibration point with real world position  $(X_w, Y_w, Z_w)_n$ , each camera sees the point on its image plane at a unique location  $(X, Y)_n$ . This transformation can be described by functions  $f_n$

$$(X, Y)_n = f_n(X_w, Y_w, Z_w, a_1, \dots, a_N), n=1,2; \quad (12)$$

Through the use of calibration points, the coefficients  $a_k$  can be determined. For the purposes of PSP, the model geometry is well defined and the displacements are small compared to the scale of the model. These conditions provide creation of linear system of equations connecting displacements in image plane  $(\Delta X, \Delta Y)_n$  with model deformations  $(\Delta X_w, \Delta Y_w, \Delta Z_w)$  in the calibration points:

$$(\Delta X, \Delta Y)_n = f_{nX} \Delta X_w + f_{nY} \Delta Y_w + f_{nZ} \Delta Z_w$$

$$n=1,2; f_{nX(Y,Z)} - \text{partial derivatives in } (X_w, Y_w, Z_w) \quad (13)$$

For data set from two cameras this over-determined linear system can be solved.

A schematic of the combined system is shown in Figure . The signal camera is placed near the nose of the model and the reference camera is placed near the tail providing a stereo view of the model. The pressure taps act as markers for the system for both the PSP resection process and for tracking model deformation. The location of the pressure taps on the model is well defined in the model geometry. The markers are located on the image bitmaps (X, Y) of each image and these bitmap coordinates are converted to physical space (X<sub>w</sub>, Y<sub>w</sub>, Z<sub>w</sub>) using the calibration. The system is calibrated by acquiring images of the model at several angles of attack. The locations of the markers were measured using a Coordinate Measurement Machine. These marker locations were used in the camera calibration process.

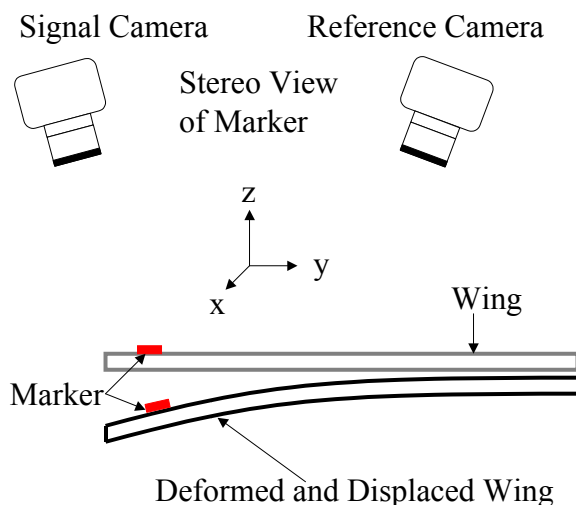


Figure 27: Stereo Model Deformation System.

## 9.0 COMBINED PSP- DEFORMATION MEASUREMENTS

The pressure coefficient for the UCAV model at Mach 0.4 and 20 degrees angle of attach is shown in Figure 28. This distribution was obtained using the Binary PSP. The defining aerodynamic features are evident in this image. The strong vortex off of the nose of the model weakens and propagates along the side of the model. Near the wing/body junction, a secondary vortex appears on the wing and sweeps outboard along the wing. After a short distance, this vortex bursts and continues to move along the span of the wing.

An estimate of the accuracy of the PSP measurements is obtained by plotting the pressure from the PSP near the taps versus the tap pressure. This data was compiled at over 40 tap locations. The mean squared deviation in this plot is about 0.1 psi, this deviation is substantially larger than that obtained by Bell using the same PSP. In this case, the major source of error is believed to be background illumination. The SARL is an open circuit tunnel and therefore, it is difficult to eliminate ambient light. For this test, only four 4-inch LED lamps were available. This level of illumination required longer exposure times and therefore, higher levels of background noise. A further complication was the variation of the background. The background varies from about 1% of camera dynamic range to over 30% of the camera dynamic range during the day. Furthermore, this background can change substantially in a short time due to cloud cover or other shadows.

## Multi-Aspect Solutions for Moving Vehicle Testing

To minimize this dynamic background effect, a background image was acquired on every fifth exposure. While these interlaced improved the signal to noise, some error remains. To minimize this problem on future tests, more lamps are required and background and data shots should be interlaced to improve signal to noise.

Deformation measurements indicate both a bulk shift of the model and bending of the wing. The bulk shift is approximately 0.6 inches and wing deformed about 0.4 inches at Mach 0.4 and 20° angle of attack. The bulk shift is a significant source of error for standard PSP as shown in Figure 9. The wing deformation of 0.4 inches is close to the value predicted for this model prior to the test.

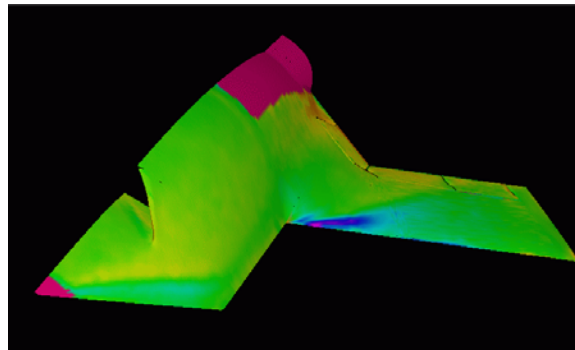


Figure 28:  $C_p$  distribution on UCAV at Mach 0.4 and 20 degree angle of attack using Binary PSP.

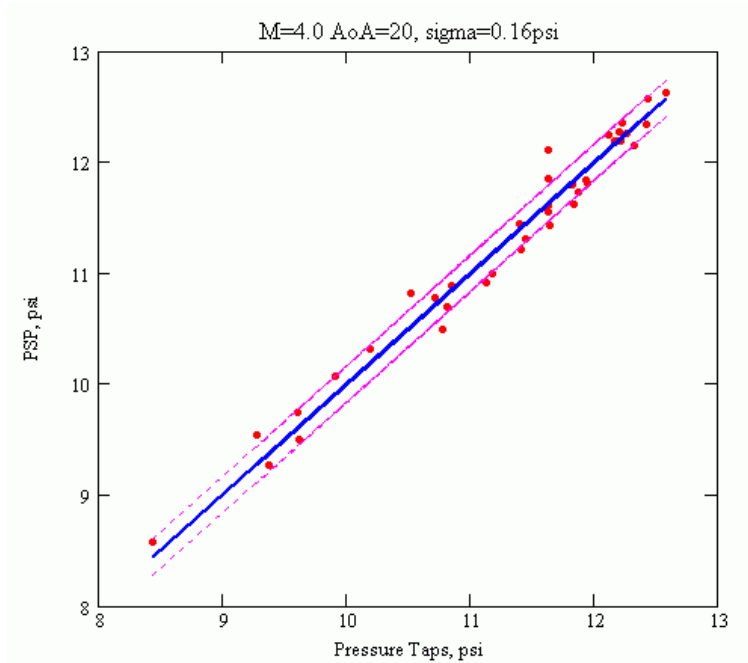


Figure 29: PSP measurement versus conventional tap pressure at 40 locations on the UCAV model.

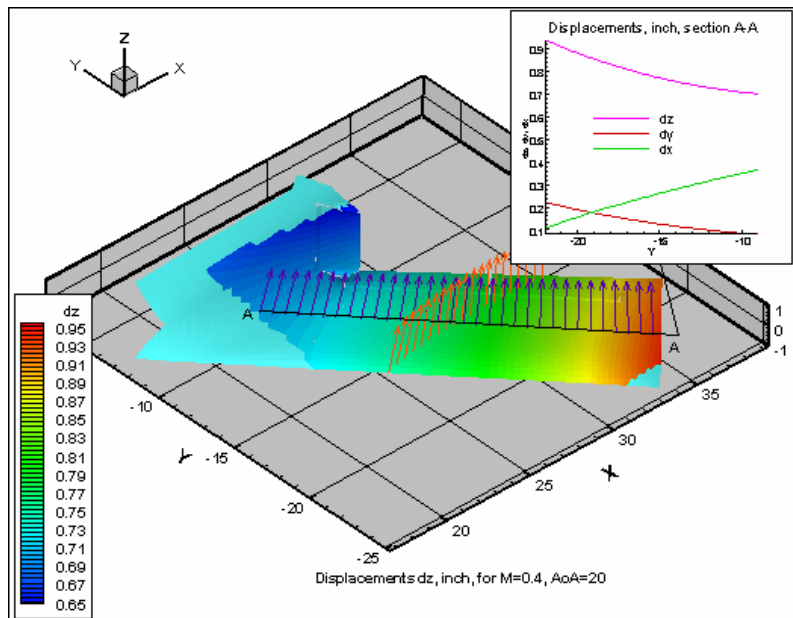


Figure 30: Displacement and Deformation of the UCAV model at 20 degree angle of attack and Mach 0.4.

## 10.0 TEMPERATURE SENSITIVE PAINT

The TSP technique allows temperature field measurements to be obtained on a vehicle model or components of real vehicles [1]. The evolution of the temperature field allows determination of a heat flux to the surface. TSP technique offers significant advantages over conventional IR techniques due to ability to suppress ambient radiation.

A typical temperature-sensitive paint (TSP) is composed of temperature-sensitive fluorescent molecule and a polymer binder. The temperature-sensitive paint method is based on the sensitivity of certain luminescent molecules to their thermal environment. Specifically, the mechanism of thermal quenching allows an excited state molecule to relax to the ground state through a non-radiative process. The result is that the luminescent signal from the painted surface is a function of temperature of that surface.

Image based temperature measurements using TSP are accomplished by coating the model surface with the TSP and illuminating the surface with light of the appropriate wavelength to excite the luminescent molecule like it is conducted for PSP measurements. The surface is imaged through a long-pass filter to separate the luminescent signal from the illumination and the luminescent signal distribution is recorded. Unfortunately, the luminescent signal from the paint is not only a function of temperature. The luminescence varies with illumination intensity, probe concentration, paint layer thickness, and detector sensitivity. These spatial variations result in a non-uniform luminescent signal from the painted surface. The spatial variations are eliminated by taking the ratio of the luminescent intensity of the paint at an unknown test condition (wind-on) with the luminescent intensity of the paint at a known reference condition (wind-off). This wind-on wind-off ratio is then converted to pressure using a previously determined calibration of the TSP.

TSP formulations based on polymeric binder can work in temperature range roughly  $-200^{\circ}\text{C}$   $-200^{\circ}\text{C}$ . Typical calibration curve for TSP is presented in Figure 31. TSP response time for thin layer with thickness several  $\mu\text{m}$  can be in microsecond region thus time resolution in TSP measurements is determined mainly by illumination and acquisition system.

## Multi-Aspect Solutions for Moving Vehicle Testing

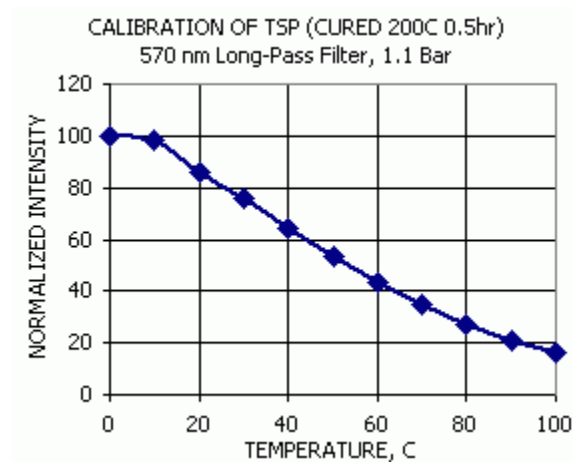


Figure 31: Typical TSP calibration.

There are several experimental examples then TSP measurements are conducted together with PSP measurements. One of the reasons is temperature compensation of the PSP data, but temperature field itself especially its time evolution provides valuable information. Data in Figure 32 presents pressure field on the sphere-sting model taken at  $M=5$ . TSP and PSP were applied on the right and left model surface. Image acquisition rate was 11 frames per second. TSP fields corresponding time 10s, 40s and 90s from flow start and temperature vs. time chart at selected point on model surface are presented in Figure 33.

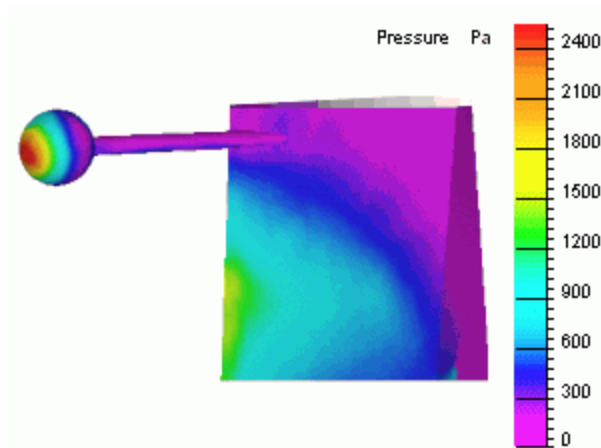


Figure 32: Pressure field, Binary PSP,  $M=5$ ,  $T_o=289K$ ,  $P_o=40KPa$ .

## 11.0 DATA PROCESSING

Experimental Flow Diagnostic requires integrated data processing solutions for PSP/TSP/S3F/etc. techniques. The next step is a combination of data processing software with computational fluid dynamics (CFD) models to provide a comprehensive understanding of the aerodynamic response of the model. The current state of development of EFD and data processing techniques allowed to develop a complete integrated

systems approach for testing and analysis including: hardware, acquisition-analysis software, comprehensive comparison with CFD predictions and using experimental results for CFD model adoption for the physical reality.

It is clear that all drawbacks of the PSP/TSP/S3F itself, light source, CCD camera, factors from the ambient flow like model displacement, temperature variation, etc. finally will be accumulated in the acquired data, mainly images, and should be resolved by data processing algorithms and efficiently processed by appropriate software in the reasonable time.

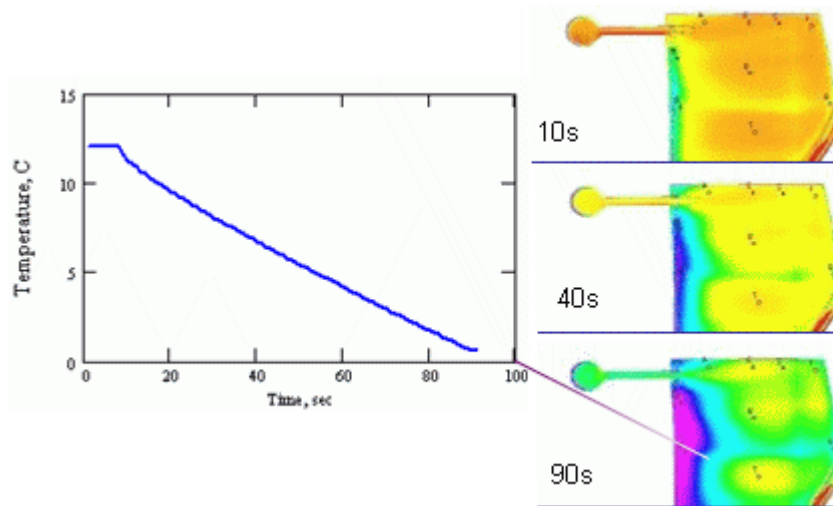


Figure 33: Temperature field evolution. TSP,  $M=5$ ,  $T_o=289K$ ,  $P_o=40KPa$ .

Huge amount of experimental data requires processing-time and user-efficient software. Standard request is results delivery in the near real time – just immediately after experiment or during experiment. This request is quite understandable – wind tunnel experiment can be very expensive and decision about next step in the experiment schedule can save a lot off many and time. By the essence PSP measurement is comparison of two (or more) luminescence distributions on the images of the model. These images are taken in different states of the flow fields around model, different forces acting on the model and as results different space position. Thus, before comparison images should be aligned or registered relative each others [3, 12]. Accuracy and efficiency of the alignment procedure is the key component of the PSP/TSP/S3D data processing. Alignment procedure is essentially estimation of local deformation field between structures on the compared images. In PSP/TSP image processing these fields are usually screened, and their efficiency determines mainly SNR on the final pressure and temperatures fields, but for S3F and stereo photogrammetry deformation field is the main output.

Algorithms for estimating the deformation image pairs are widely used in many fields, including Particle Image Velocimetry, Machine Vision etc. An extensive review of the different techniques is given by Brown [20]. S<sup>3</sup>F measurements require high precision to evaluate the displacement vectors with reasonable robustness against noise--similar to PIV particle images with high seed densities. The techniques developed for the image alignment in PSP/TSP experiments was adopted for use with the S<sup>3</sup>F technique. This algorithm is a hybrid, using phase correlation [7] to estimate integer (in pixels) part of the displacement vector and an optical-flow based method to estimate the sub-pixel part of the displacement.

Phase-correlation image registration method is based on the properties of the Fourier transform applied to two images that are shifted relative to each other. The Fourier transform of an image  $f(x,y)$  is a complex function which can be expressed in exponential form:

## Multi-Aspect Solutions for Moving Vehicle Testing

$$F(\omega_x, \omega_y) = |F(\omega_x, \omega_y)| e^{i\phi(\omega_x, \omega_y)} \quad (14)$$

where  $|F(\omega_x, \omega_y)|$  is the magnitude of the Fourier transform and  $\phi(\omega_x, \omega_y)$  is the phase angle. Phase correlation relies on the translation property of the Fourier transform sometimes referred to as the Shift Theorem. Given two images  $f_1$  and  $f_2$  which differ only by a displacement  $(d_x, d_y)$ , i.e.  $f_2(x, y) = f_1(x - d_x, y - d_y)$ , their corresponding Fourier transforms  $F_1$  and  $F_2$  will be related by Eq. (2)

$$F_2(\omega_x, \omega_y) = e^{-i(\omega_x d_x + \omega_y d_y)} F_1(\omega_x, \omega_y) \quad (15)$$

If the cross-power spectrum of the two images is computed, the Shift Theorem guarantees that the phase of the cross-power spectrum is equivalent to the phase difference between the images.

$$\frac{F_1(\omega_x, \omega_y) F_2^*(\omega_x, \omega_y)}{|F_1(\omega_x, \omega_y) F_2^*(\omega_x, \omega_y)|} = e^{i(\omega_x d_x + \omega_y d_y)} \quad (16)$$

By taking the inverse Fourier transform of the cross-power spectrum the displacement will be represented by an impulse at the corresponding coordinates. Since the phase difference for every frequency contributes equally, the location of the peak will not be strongly affected by narrow-bandwidth noise, which may be the case for conventional cross-correlations.

Several authors [21, 22] have studied similar methods in the evaluation of sub-pixel displacements. Particularly, Sjordahl [22] analyzed the effects of noise and rotation on the accuracy of determining displacements in speckle photography. In general, it is possible to obtain a subpixel estimation of the displacement by calculating the centroid of the cross-correlation or phase-correlation peak.

For our algorithm, a different approach was used for estimating the sub-pixel displacement. It was found that the following method provided better stability against noise for S<sup>3</sup>F applications (a similar algorithm was proposed by Cheng-Yuan, et al. [21])

Optical Flow & Phase Correlation technique [23-27] includes the following steps:

- In the first stage, the displacement is estimated with either a phase or cross-correlation algorithm, with a precision of 1 pixel.
- In the second stage, the residual displacement is evaluated using a method similar to the optical flow calculation of Cheng-Yuan, et al.,<sup>21</sup>.

$$I_2(x, y) = I_1(x + d_x, y + d_y) = I_1(x, y) + \text{grad}I_1(x, y) \cdot (d_x, d_y) \quad (17)$$

- The sub-pixel displacement is then found using a least-square approximation:

$$(d_x, d_y) = \arg \min_{(d_x, d_y)} \left( I_2(x, y) - I_1(x, y) - \text{grad}I_1(x, y) \cdot (d_x, d_y) \right)^2 \quad (18)$$

- For computations, the gradient  $\text{grad}I_1(x, y)$  is evaluated using a convolution of the original image  $I_1$  with Gaussian gradient filters (one for each direction). By varying the parameter  $\sigma$  of the Gaussian kernel, it is possible to vary the sensitivity of the method to noise.

In the actual data-processing images in wind-off and wind-on condition are divided into areas of interrogation (cells). For each pair of cells phase-correlation and optical flow algorithm is applied, producing one 2D vector. Resulting vector field may-be filtered and interpolated.

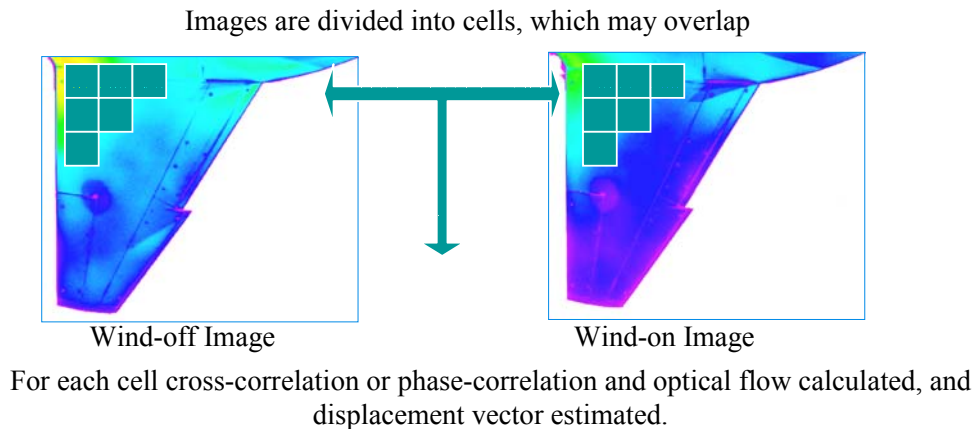


**Figure 34: Data processing flow.**

The sensitivity to the local variations in the displacement field depends on the size of the cell, and the distance between their centers. Unfortunately, the maximum displacement is limited by the size of cell. Sometimes, to achieve the required sensitivity and magnitude of the displacements, it is necessary to implement this technique in several hierarchical iterations [27].

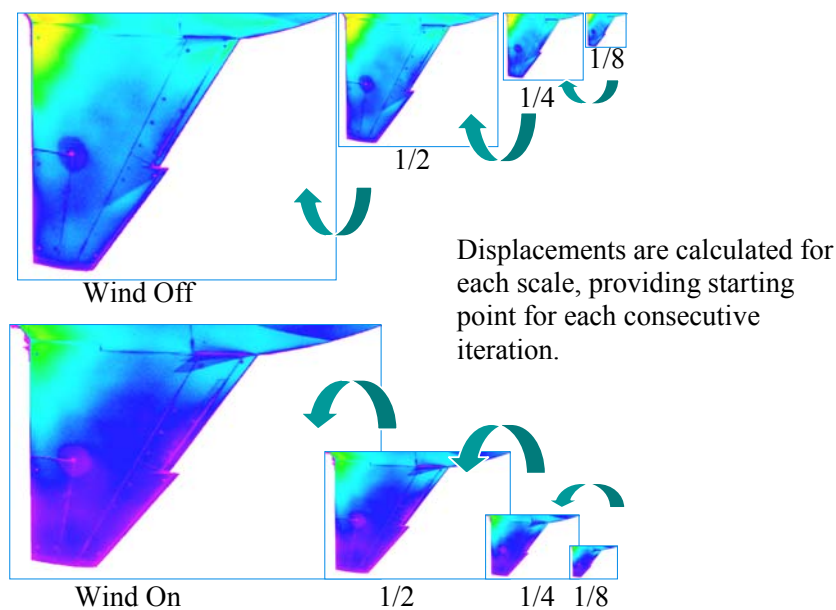


**Figure 35: Hierarchical calculations of the displacement vectors.**

The new algorithm was tested on images obtained with a PSP imaging system, using synthetic random patterns (0), under linear and rotation translations (0). Images were processed with the hybrid (Phase Correlation + Optical Flow) algorithm and the Phase-Correlation (only) based algorithm. The results of this comparison shown in Figs. 8-10, demonstrated a significant improvement in the accuracy for some cases.

## Multi-Aspect Solutions for Moving Vehicle Testing

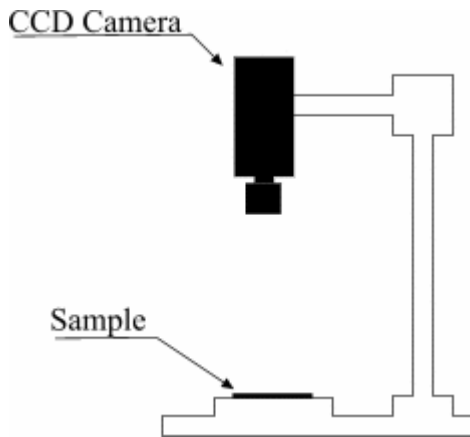


Figure 36: Test setup.

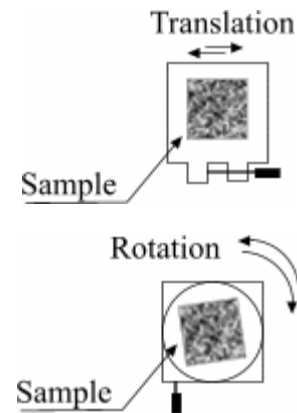


Figure 37: Test cases.

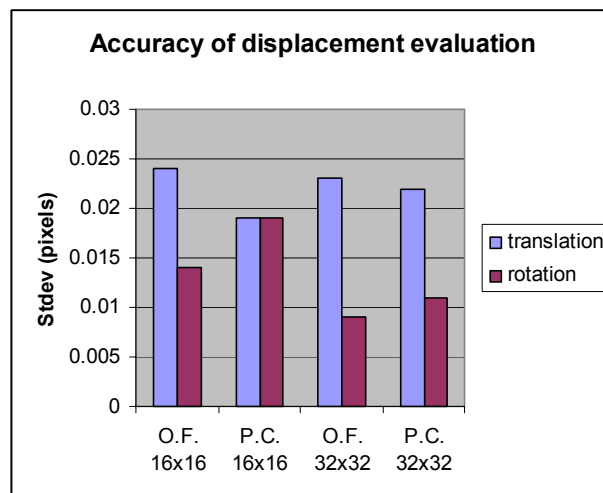


Figure 38: Standard deviation of displacement evaluation for hybrid algorithm (O.F.) and Phase Correlation centroid algorithm (P.C.) showed for cells 16x16 pixels and 32x32 pixels.

Optical Flow plus Phase Correlation Algorithm (OFPCA) significantly (about 5-10 times) improved dynamic range of S3F and model deformation measurements.

Figure 39 illustrates pressure and shear force fields measurements on the plate under action of low speed jet. S3F with the thickness 1mm and shear modulus  $\mu=270$  Pa was applied on the surface. Nozzle with internal diameter 2mm and axis inclined at the angle  $40^\circ$  creates low speed jet flow. Normal component of deformation field was measured using information from luminescence output and shear components using OFPCA. CCD camera with resolution 1280 by 1024 pixel in combination with OFPCA provided shear displacement measurement with resolution 0.1 $\mu$ m (cell window 32 by 32 pixel) in dynamic range  $\pm 10$ mkm. Results of post-processing compared with pressure taps data show that pressure field can be measured with resolution defined by SNR about 3-5 Pa for this S3F composition.

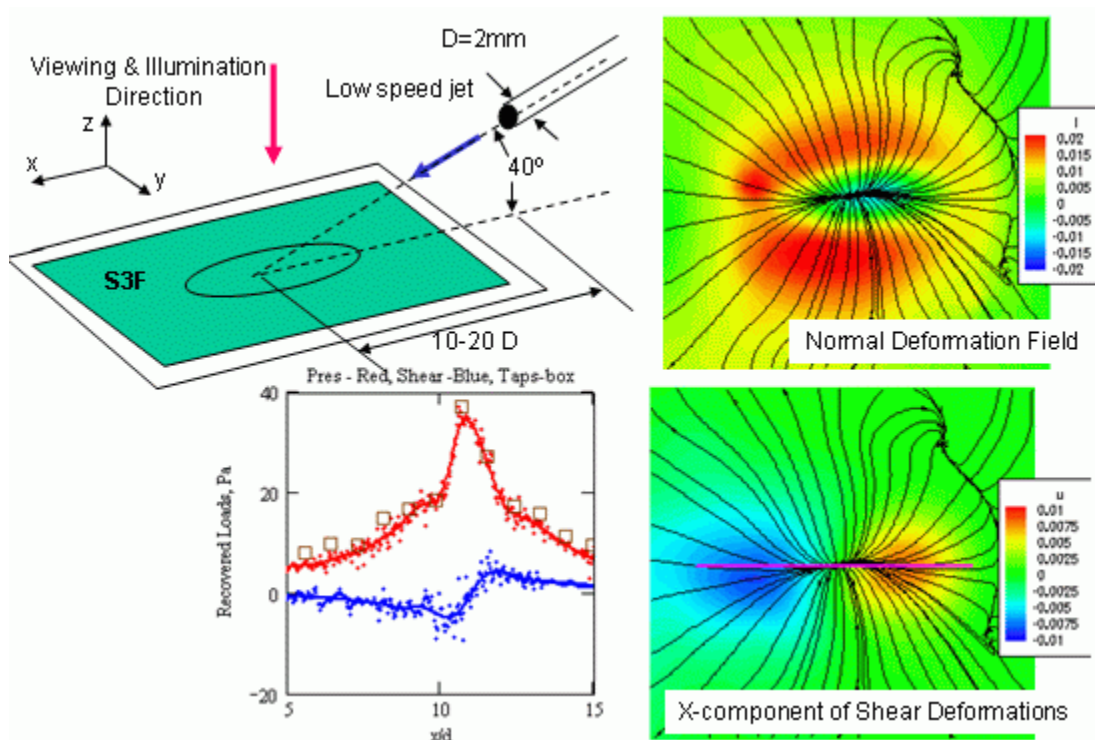


Figure 39: Measurements of pressure and shear force distributions using S3F.

## 12.0 CONCLUSIONS

Considered PSP, TSP, S<sup>3</sup>F and stereo photogrammetry methods provide significant impact in flow diagnostic on the model surface. It is demonstrated that main drawbacks of PSP technique like temperature sensitivity and model deformations can be overcome using temperature compensated bi-luminophore PSP. S<sup>3</sup>F technique provides possibility significantly increase sensitivity of pressure measurements and obtain pressure and friction force distributions with resolution up to parts of Pascal.

Information about model deformations can be extracted concurrently with PSP measurements using photogrammetry approach. Combination of Phase correlation and Optical Flow techniques provides measurements of image deformation field with standard deviation about 0.01-- 0.02 pixel.

## 13.0 REFERENCES

- [1]. T. Liu, Campbell, B., Burns, S. Sullivan, J., "Temperature and Pressure-Sensitive Paints in Aerodynamics", Applied Mechanics Reviews, Vol. 50, No. 4, 1997, pp. 227-246.
- [2]. Liu., T., Guille, M., Sullivan, J. P., "Accuracy of Pressure Sensitive Paint", AIAA Journal, Vol. 39, No. 1.
- [3]. Bell, J.H., McLachlan, B.G., "Image Registration for Pressure-Sensitive Paint Applications", Experiments in Fluids, Vol. 22, No. 1, 1996, pp. 78-86.

## Multi-Aspect Solutions for Moving Vehicle Testing

---

- [4]. Liu, T., Cattafesta III L.N., Radeztsky R.H, Burner, A.W., “Photogrammetry Applied to Wind-Tunnel Testing”, AIAA Journal, Vol. 38, No. 6, June 2000, pp. 964-971.
- [5]. Fleming, G.A., Gorton,S.A., “Measurements of rotorcraft blade deformation using Projection Moire Interferometry”, Journal of Shock and Vibration, Vol. 7, No. 3, 2000.
- [6]. Puklin, E., Carlson, B., Gouin, S., Costin, C., Green, E., Ponomarev, S., Tanji, H., Gouterman, M., “Ideality of Pressure-Sensitive Paint. I. Platinum Tetra(pentafluorophenyl)porphine in Fluoroacrylic Polymer”, Journal of Applied Polymer Science, Vol. 77, 2000, pp. 2795-2804.
- [7]. White, F. M., “Viscous Fluid Flow”, 2<sup>nd</sup> ed., McGraw-Hill, 1991.
- [8]. Optrod Binary paint. [www.optrod.com](http://www.optrod.com)
- [9]. ISSI Binary paint. [www.innssi.com](http://www.innssi.com)
- [10]. J.W. Naughton, M. Sheplak “Modern Development in Shear Stress Measurement”, Progress in Aerospace Sciences 38(2002) 515-570.
- [11]. Bell James H et al. “Surface Pressure Measurements Using Luminescence Coatings” Annual Rev. Fluid Mech. 2001. 33:155-206.
- [12]. Mosharov V, Radchenko V, Fonov S. “Luminescent Pressure Sensors in Aerodynamic Experiment”, Moscow: TsAGI, CWA Int. Corp. 1997.
- [13]. Reda D.V. “Measurements of continuous pressure and shear distributions using coating and imaging techniques”, AIAA Journal v.36, pp. 895-899, 1998.
- [14]. Zhong, S. “Detection of flow separation and reattachment using shear-sensitive liquid crystals”, Experiment in Fluids, v.32 pp.667-673, 2002.
- [15]. Tarasov V.N, Orlov A.A. “Method for determining shear stress on aerodynamic model surface”, Patent of Russia, 4841553/23/1990.
- [16]. Tarasov V., S. Fonov, A. Morozov, "New gauges for direct skin friction measurements." Proc. Of 17<sup>th</sup> International Congress on Instrumentation in Aerospace Simulation Facilities (ICIASF), Monterey, California, 29 Sept to 2 Oct 1997.
- [17]. Landau L.D, Lifshits E.M. “Course of Theoretical Physics: Theory of Elasticity”, Vol. 7 Butterworth-Heinemann, 1995, 260pp.
- [18]. Braess D. “Finite Element”, Second Edition, Cambridge University Press, 2001.
- [19]. Fonov S. D. et al. 2004 NEW METHOD FOR SURFACE PRESSURE MEASUREMENTS. Flow-Visualization Conference, University of Notre Dame, Indiana, USA 2004.
- [20]. Brown L. G. 1992 “A Survey of Image Registration Techniques” ACM Computing Surveys, Vol 24, No. 4, December 1992.

- [21]. Cheng-Yuan Tang, Yi-Ping Hung, and Zen Chen. "Robust two-stage approach for image motion estimation", Electronics Letters, Vol. 34, No. 11, pp. 1091-1093, May 1998.
- [22]. Sjodahl M. 1994 Electronic speckle photography: increased accuracy by nonintegral pixel shifting. Applied Optics, 1 October 1994, Vol. 33, No. 28.
- [23]. Barron J. L., Fleet D. J., Beauchemin S. S., and Burkitt T. A.. Performance of optical flow techniques. IEEE Computer Society Conference on Computer Vision and Pattern Recognition, 1992.
- [24]. Fonov V.S. Development and Analysis of Data Processing Methods Applied to Luminescent Coating Systems in Aerodynamics. PhD thesis Heriot-Watt University 2002.
- [25]. Shekarforoush H., Berthod M., and Zerubia J. 1996 Subpixel image registration by estimating the polyphase decomposition of cross power spectrum. In Computer vision and pattern recognition, pp. 532-537, Los Alamitos, CA, 1996. IEEE computer society press.
- [26]. Black M. J. Anadan P. A. 1993 Framework for the robust estimation of Optical Flow. Presented at 4th international conference on computer vision 1993 (ICCV93).
- [27]. Olsen O. F. 1996 Multi-Scale Segmentation of Grey-Scale Images. Technical Report DIK U-96-30 August 1996.



**Multi-Aspect Solutions for Moving Vehicle Testing**

---

